



Technical Note

Improving the spatial resolution of magnetic resonance inverse imaging via the blipped-CAIPI acquisition scheme



Wei-Tang Chang^{a,b,1}, Kawin Setsompop^{a,1}, Jyrki Ahveninen^a, John W. Belliveau^{a,c}, Thomas Witzel^a, Fa-Hsuan Lin^{b,*}

^a Athinoula A. Martinos Center for Biomedical Imaging, Department of Radiology, Massachusetts General Hospital/Harvard Medical School, Charlestown, MA, USA

^b Institute of Biomedical Engineering, National Taiwan University, Taipei, Taiwan

^c Harvard-MIT Division of Health Sciences and Technology, Cambridge, MA, USA

ARTICLE INFO

Article history:

Accepted 19 December 2013

Available online 27 December 2013

Keywords:

Inverse imaging

Parallel imaging

Blip

CAIPIRINHA

ABSTRACT

Using simultaneous acquisition from multiple channels of a radio-frequency (RF) coil array, magnetic resonance inverse imaging (InI) achieves functional MRI acquisitions at a rate of 100 ms per whole-brain volume. InI accelerates the scan by leaving out partition encoding steps and reconstructs images by solving under-determined inverse problems using RF coil sensitivity information. Hence, the correlated spatial information available in the coil array causes spatial blurring in the InI reconstruction. Here, we propose a method that employs gradient blips in the partition encoding direction during the acquisition to provide extra spatial encoding in order to better differentiate signals from different partitions. According to our simulations, this blipped-InI (bInI) method can increase the average spatial resolution by 15.1% (1.3 mm) across the whole brain and from 32.6% (4.2 mm) in subcortical regions, as compared to the InI method. In a visual fMRI experiment, we demonstrate that, compared to InI, the spatial distribution of bInI BOLD response is more consistent with that of a conventional echo-planar imaging (EPI) at the level of individual subjects. With the improved spatial resolution, especially in subcortical regions, bInI can be a useful fMRI tool for obtaining high spatiotemporal information for clinical and cognitive neuroscience studies.

© 2013 Elsevier Inc. All rights reserved.

Introduction

The acquisition time for whole-brain magnetic resonance imaging (MRI) data is limited by the time required to traverse the k -space. The data acquisition can be completed by either in a set of 2D k -space trajectories across slices or in a single 3D k -space trajectory covering the whole imaging volume. Conventional functional MRI (fMRI) (Belliveau et al., 1991) using blood-oxygen-level-dependent (BOLD) contrast (Kwong et al., 1992; Ogawa et al., 1990) is usually accomplished by the echo-planar imaging (EPI) (Mansfield, 1977). Considering the state-of-the-art gradient slew rate and maximal strength, EPI can complete the 2D k -space traversal in approximately 40 ms per slice or 2 s with the whole brain coverage. The quest for higher temporal resolution in fMRI has been motivated by its potential to detect and to suppress physiological fluctuations in order to increase the sensitivity of detecting brain activity (Kruger and Glover, 2001; Lin et al., 2012). Likewise, high-speed echo-volumar image (EVI) integrated with parallel imaging could resolve the physiological signal fluctuation to increase the sensitivity in event-related fMRI (Posse et al., 2012; Witzel et al., 2011,

2008). In addition, higher temporal resolution of fMRI has been suggested to be beneficial for improving the power of detecting neuronally related timing information and connectivity among brain areas (Deshpande et al., 2010; Feinberg et al., 2010; Kayser et al., 2009; Lee et al., 2013; Lin et al., 2013; Roebroeck et al., 2005).

One approach in accelerating the fMRI data acquisition is to optimize the k -space trajectory and the corresponding reconstruction method. This can be achieved by using partial k -space sampling (Feinberg et al., 1986; McGibney et al., 1993), compressed sensing (Lustig et al., 2007), or exploiting a priori information (Tsao et al., 2001), such as key-hole imaging (Jones et al., 1993; van Vaals et al., 1993) and singular-value-decomposition MRI (Zientara et al., 1994). As the technology of radio-frequency (RF) receiver coil array advances, parallel MRI methods, which simultaneously acquire MRI data from multiple channels of RF coil array, have become a method of reducing the scanning time. Parallel MRI methods, such as the k -space SMASH (Sodickson and Manning, 1997) and GRAPPA (Griswold et al., 2002), or the image domain SENSE (Pruessmann et al., 1999) method, reduce the acquisition time by reducing the k -space traversal at a cost of reduced signal-to-noise ratio (SNR). In fMRI, parallel MRI has been successfully combined with the gradient-echo EPI to achieve accelerated acquisitions (Preibisch et al., 2003; Schmidt et al., 2005). It has also been demonstrated that incorporating static a priori information can further improve the sensitivity of fMRI (Lin et al., 2005).

* Corresponding author at: Institute of Biomedical Engineering, National Taiwan University, Taipei, Taiwan. Fax: +886 2 33665268.

E-mail address: fhlin@ntu.edu.tw (F.-H. Lin).

¹ Wei-Tang Chang and Kawin Setsompop contributed equally to this work.

The inverse imaging (InI) method (Lin et al., 2006) is a further generalized parallel MRI method for 3D volumetric acquisition by leaving out all partition-encoding steps. Consequently, the volumetric brain is projected along the partition-encoding direction onto a single plane. InI is closely related to the MR-encephalography (Hennig et al., 2007). InI reconstructs a 3D image from a set of 2D projection images from different channels of an RF coil array using the coil sensitivity information. Mathematically, the image reconstruction is performed by solving a set of underdetermined linear systems. Combined with the echo shifting technique (Chung and Duerk, 1999), the sampling rate of whole-brain InI can become as high as 40 Hz (Chang et al., 2013). While InI allows for a very high temporal resolution, the attainable spatial resolution depends on the available spatial information in the RF coil array. Correlated coil spatial information will cause spatial blurring in the InI reconstruction. One strategy to improve the spatial resolution is through the use of a more sophisticated reconstruction algorithm, such as reconstructing the images in k -space (Lin et al., 2010) or using spatial filtering (Lin et al., 2008; Liou et al., 2011). Another strategy is to modify the data acquisition by collecting data from multiple projections instead of one single projection (Tsai et al., 2012).

In this study, we aim to improve the spatial resolution of InI by modifying the spatial encoding in the pulse sequence. Specifically, InI was integrated with the “blipped-CAIPI” acquisition (Setsompop et al., 2012) to create the “blipped-InI” (bInI) method. The blipped-CAIPI technique has been used in the Simultaneous MultiSlice (SMS) acquisition, which spatially shifts the aliasing patterns of simultaneously acquired slices. This is achieved by applying additional slice-selection gradient blips concurrently with the EPI phase-encoding blips. The additional slice-selection gradient blip provides additional encoding that helps differentiate signal from different slices and thereby reduces the noise amplification (g -factor) penalty. In this work, we applied the blipped-CAIPI acquisition concept to InI in order to reduce spatial blurring. In the following sections, we first introduced the bInI acquisition and reconstruction method. We then quantitatively characterized the spatial resolution and localization accuracy of bInI using synthetic data. Finally, we performed in vivo experiments of event-related BOLD fMRI using bInI. These BOLD responses were then compared with the BOLD responses obtained from standard EPI and InI experiments. The simulation results suggested that, compared to InI, bInI can improve the spatial resolution up to 33% and localization accuracy more than 100% in subcortical regions. Compared to InI, the fMRI experimental results using bInI showed improvement in the robustness of activation maps.

Theory

Pulse sequence of blipped InI

Without losing generality, we use x , y , and z axes to represent the axis along read-out, phase-encoding, and partition-encoding directions, respectively. Fig. 1(a) shows the pulse sequence diagram of the bInI,

where α denotes the flip angle. This pulse sequence diagram is similar to the conventional single-slice 2D EPI acquisition, except additional partition-encoding gradient (G_z) blips and slab-selective RF pulse. These additional G_z blips are of the same patterns to the ones used in the blipped-CAIPI acquisition sequence for the Simultaneous MultiSlice (SMS) acquisition (Setsompop et al., 2012). These G_z blips are in synchrony with the phase-encoding gradient (G_y) blips in order to provide extra spatial encoding along the z axis. Two variants of G_z blips are shown in Figs. 1a and b, which achieve in-plane shift of FOV/2 (Fig. 1a) and FOV/3 (Fig. 1b). The gradient moment of the G_z blips in the bInI pulse sequence can be expressed as

$$\beta \Delta k_z = \beta \cdot (2\pi / (\gamma \cdot \text{FOV}_z)), \quad (1)$$

where β denotes a real-number scale factor, γ denotes the gyromagnetic ratio, and FOV_z denotes the length along partition encoding direction. Δk_z is the minimum spacing in k -space along the k_z direction.

For the SMS acquisition, the G_z blip encoding creates an inter-slice image shift along the phase encoding (PE) direction between simultaneously excited slices (Breuer et al., 2005; Lee et al., 1995; Setsompop et al., 2012). The effect of this blip encoding on volumetric bInI is different from the multi-slice acquisition. Fig. 2 shows the principle of bInI encoding for the case of in-plane FOV/2 shift and $|\beta|$ of 1. The red dashed lines in the left-most image in Fig. 2a delineate image partitions (obtained after all partition encoding steps). Since G_z blips always have zero gradient moments in odd phase encoding lines, the G_z blips only introduce phases in even phase encoding lines. Moreover, different phase offsets are introduced by the G_z blips in the even k -space lines for different partitions. Considering the case that the partition s2 is at the scanner iso-center and thus has no phase offset. On the contrary, G_z blips introduce $-\pi/4$ and $\pi/4$ at partitions s1 and s3 respectively, which are at the position 3/8 and 5/8 of the FOV in the partition encoding direction. These phase modulations on different phase encoding lines of the different partitions are marked at the right margin of s1, s2, and s3 panels in Fig. 2a. In the image space, these k -space phase modulations cause spatial shifts of FOV/2 along the phase encoding direction for all partitions but with different weighting for different partitions, as shown in Fig. 2b. The top row in Fig. 2b shows the images in representative partitions without the phase modulation introduced by G_z blips. The middle row shows the phase offsets introduced by G_z blips. The modulated slice images are shown in the bottom row. Using such G_z blips, strong $N/2$ ghost is observed in the partitions toward the edge of the excitation volume, while central slices show relatively weak $N/2$ ghost. In accelerated bInI acquisition, all the partition encoding steps are removed and consequently all the partitions are integrated, as shown in the right-most images in Fig. 2b. Note that the similar analysis principal can be applied to other type of shifts such as FOV/3.

As the SMS method can be formulated as a 3D encoding framework (Zahneisen et al., 2013), the concept of bInI can be understood in 3D k -space as well. Fig. 3 shows the k -space trajectories of InI and blipped

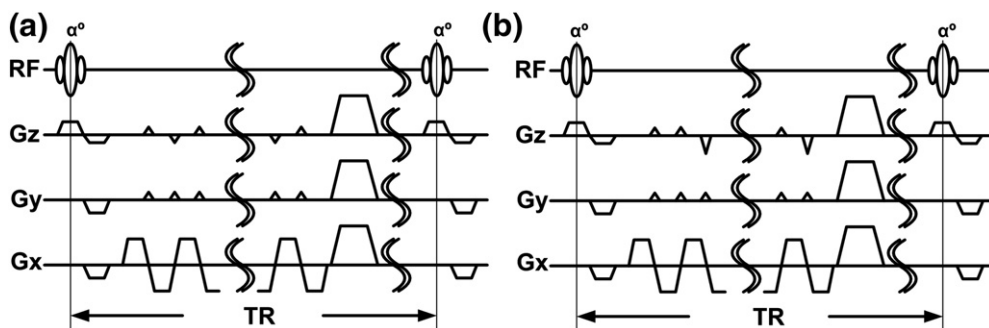


Fig. 1. The blipped-InI pulse sequences to achieve (a) FOV/2 and (b) FOV/3 in-plane shifts. In (a), the G_z blips change the polarity alternatively between read-outs but have the same magnitude of gradient moment. Such G_z blips can induce FOV/2 in-plane shift. In (b), the G_z blips have the repetitive “up-up-down” pattern across read-outs. The downward G_z blips have twice the gradient moment of the upward G_z blips. Such G_z blips can introduce FOV/3 in-plane shift.

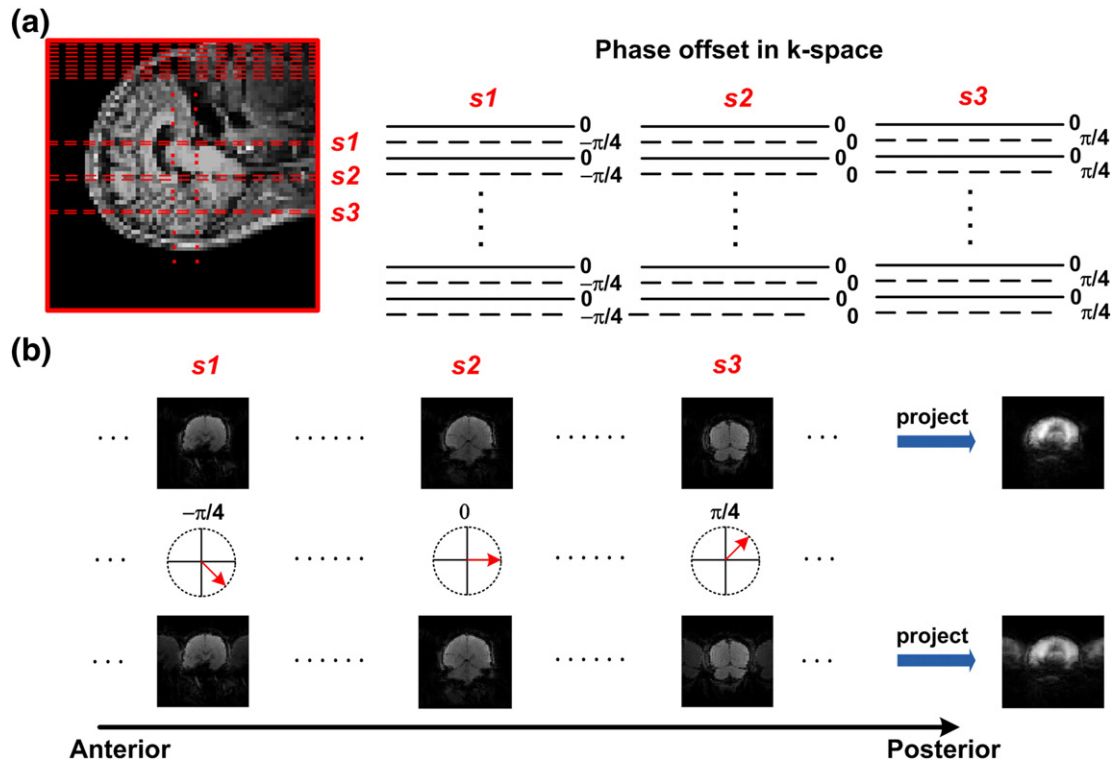


Fig. 2. Illustration of the principle of the blipped-InI method. The red-dashed line in the left-most panel in (a) delineates the boundaries of different partitions. s_1 , s_2 and s_3 denote the partitions at a distance of $FOV_z \times 3/8$, $FOV_z/2$ and $FOV_z \times 5/8$ from the top, respectively. The iso-center is at $FOV_z/2$. The three panels on the right in (a) show the phase offset induced by the $FOV_z/2$ shift's G_z blips in k-space. The black solid lines and dashed lines represent the odd and even k-space lines respectively. In (b), the top row shows the coronal slices from anterior to posterior without blips. The projection image shown at the right is the summation of all the slices. The middle row indicates the blip-induced phase offset at different slices. The bottom row shows the slice images after the phase-offset modulation. In the blipped-InI acquisition, all the slice images in the bottom row are projected onto one plane as shown in the bottom-right.

InI in k_y – k_z plane. The circles represent the fully sampled k-space lines along k_x -dimension (readout). The white dots represent the skipped k-space lines and black dots represent the acquired ones. The 3D k-space pattern of InI is a k_x – k_y plane while the pattern of blipped InI is in zig-zag shape. Although the blipped size $\beta\Delta k_z$ in Fig. 3 is $1 \cdot \Delta k_z$, β can be set as any other value. The spatial encoding in k_z direction provides bInI extra spatial information to reconstruct the full 3D k-space data.

Blipped-InI reconstruction

The raw data acquired from each channel of the coil array was first reconstructed using a standard 2D Fourier transformation, resulting in a time series of complex-valued projection images (similar to the one shown at the bottom right of Fig. 2b). Next, we employed the DRIFTER algorithm (Särkkä et al., 2012) to estimate and to separate the cardiac (0.75 Hz–2.5 Hz) and respiratory (0.083 Hz to 0.5 Hz) fluctuations

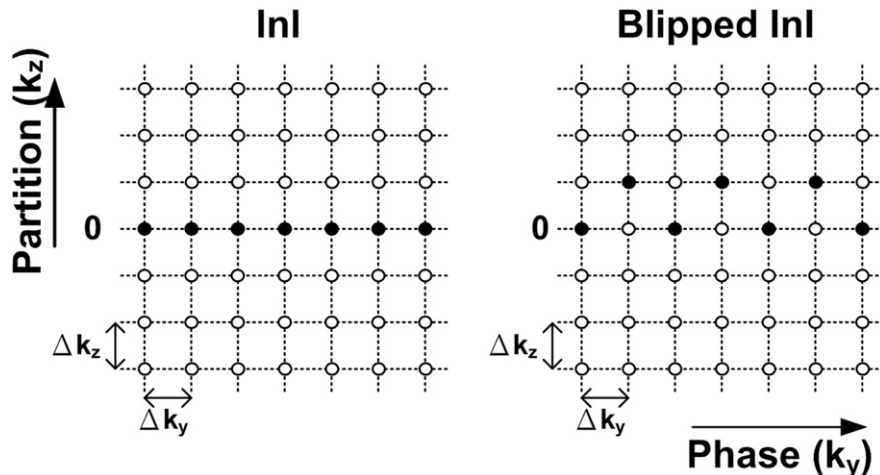


Fig. 3. K-space sampling pattern of InI and bInI. Each circle represents the fully sampled k-space line along k_x -dimension (readout). The black circles represent the acquired k-space lines while the white circles represent the skipped ones.

from the fMRI signal. Volumetric spatial reconstruction was performed after suppressing physiological noises. The previously proposed InI acquisition method (Lin et al., 2008) causes each vector consisting of image pixels of the same frequency/phase encoding but different partition encoding integrated into one projection voxel. These projection voxels are independent to each other, and can be reconstructed independently. However, in bInI, projection voxels are mutually dependent because of the different introduced spatial shifts along the phase encoding direction in different partitions (as shown in Fig. 2). This causes a single voxel in 3D is related to multiple phase encoding and partition encoding positions in the accelerated projection image. Hence, spatial reconstruction should be performed with the consideration of such correlation. Specifically, for a projection image at time instant t , we cascaded all phase encoding image voxels with their frequency encoding index x_i ($1 \leq x_i \leq N_x$) from all channels in a coil array into one $[N_y \times n_c]$ -by-1 vector $\mathbf{y}(t)$, where N_y denotes the number of image pixels along the phase encoding direction and n_c denotes the number of channels in an RF coil array. Each image plane consisting of the same frequency encoding indices but different phase encoding and partition encoding indices can be reconstructed independently. To simplify the notation, we leave out the explicit x-coordinate dependency (x_i) in the following description. The vector $\mathbf{y}(t)$ is linearly related to the image vector to be reconstructed

$$\mathbf{y}(t) = \mathbf{A}\mathbf{s}(t) + \mathbf{n}(t), \quad (2)$$

where $\mathbf{s}(t)$ is a $[N_y \times N_z]$ -by-1 image vector to be reconstructed, and $\mathbf{n}(t)$ is a $[N_y \times n_c]$ -by-1 vector denoting the contamination noise. The matrix \mathbf{A} is a $[N_y \times n_c]$ -by- $[N_y \times N_z]$ forward matrix, mapping the signals from the phase-partition encoding (y-z) plane to one vector of observed signal in the accelerated image across n_c -channel in the coil array.

The forward matrix \mathbf{A} consists of three components: spatial integration along the partition encoding direction due to leaving out partition encoding steps in the accelerated acquisition (projection matrix), spatial encoding due to G_z blips, and RF coil sensitivity. Let \mathbf{A}_c denotes a part of the forward matrix related to channel c_i , $1 \leq i \leq n_c$. \mathbf{A}_c can be written explicitly as a product of three matrices

$$\mathbf{A}_{c_i} = \mathbf{A}_{c_i}^{proj} \mathbf{A}_{c_i}^{blip} \mathbf{A}_{c_i}^{coil}, \quad (3)$$

where $\mathbf{A}_{c_i}^{proj}$ denotes a spatial projection matrix, $\mathbf{A}_{c_i}^{blip}$ denotes a G_z -blip encoding matrix, and $\mathbf{A}_{c_i}^{coil}$ denotes a RF coil sensitivity matrix. The coil-sensitivity matrix $\mathbf{A}_{c_i}^{coil}$ is diagonal with dimension of $[N_y \times N_z]$ -by- $[N_y \times N_z]$. Diagonal elements of $\mathbf{A}_{c_i}^{coil}$ can be empirically measured by the InI reference scan. The aliasing matrix $\mathbf{A}_{c_i}^{blip}$ describes the blip encoding introduced by z blips and can be derived either theoretically from a given blip encoding scheme or empirically from InI reference scans in order to account for possible imperfection in gradient encoding. The dimension of $\mathbf{A}_{c_i}^{blip}$ is $[N_y \times N_z]$ -by- $[N_y \times N_z]$. The first step in deriving $\mathbf{A}_{c_i}^{blip}$ is to calculate the phase modulation in the k -space for each partition. With the empirical approach, we started from the full 3D k -space data of bInI and InI reference scans (with all partition encoding steps). The phase modulation can then be estimated by subtracting the phase of the even k -space lines between InI and bInI data. To achieve a good estimate, only the central two even k -space lines were used because they had higher SNR. With the theoretical approach, the phase modulation (at even phase encoding lines) at partition z_i can be calculated as

$$\theta_{z_i} = 2\pi \cdot \beta \cdot d_{z_i} / FOV_z \quad (4)$$

where d_{z_i} denotes the distance away from the iso-center in the partition encoding direction and $z_i = 1, \dots, N_z$, which denotes the number of partitions. In this study, we found marginal differences in phase introduced by z blips based on these two approaches.

Let $\mathbf{k}_{z_i}^{InI}$ and $\mathbf{k}_{z_i}^{bInI}$ denote N_y -by-1 data vectors of InI and bInI in hybrid space at partition encoding index z_i , respectively. The hybrid space here is defined as the 3D space with y dimension in frequency domain and x and z dimensions in image domain. The $\mathbf{k}_{z_i}^{bInI}$ and $\mathbf{k}_{z_i}^{InI}$ are related to each other as

$$\mathbf{k}_{z_i}^{bInI} = \Theta_{z_i} \circ \mathbf{k}_{z_i}^{InI}, \quad (5)$$

where \circ denotes the element-by-element product (Hadamard product) between two vectors. Θ_{z_i} denotes the vector of complex phase offsets. For the case of FOV/2, the odd and even elements of Θ_{z_i} are 1 s and $e^{j\theta_{z_i}}$ respectively. For the case of FOV/3, likewise, the $(3p+1)^{th}$, $(3p+2)^{th}$, $(3p+3)^{th}$ elements ($p = 0, 1, 2, \dots$) are 1 s, $e^{j\theta_{z_i}}$ and $e^{j2\theta_{z_i}}$ respectively. After discrete Fourier transform, Eq. (5) becomes

$$\mathbf{p}_{z_i}^{bInI} = \text{FFT}\{\Theta_{z_i}\} \otimes \mathbf{p}_{z_i}^{InI}, \quad (6)$$

where $\mathbf{p}_{z_i}^{bInI}$ and $\mathbf{p}_{z_i}^{InI}$ denote image vectors of bInI and InI, respectively. $\text{FFT}\{\bullet\}$ denotes the discrete Fourier transform and \otimes denotes circular convolution. Mathematically, the circular convolution operation can also be rewritten as a matrix-vector product

$$\mathbf{p}_{z_i}^{bInI} = \text{FFT}\{\Theta_{z_i}\} \otimes \mathbf{p}_{z_i}^{InI} = \mathbf{A}_{c_i, z_i}^{blip} \cdot \mathbf{p}_{z_i}^{InI} \quad (7)$$

where $\mathbf{A}_{c_i, z_i}^{blip}$ denotes the blip encoding matrix at partition z_i with dimension of N_y -by- N_y . By simply replacing $\mathbf{p}_{z_i}^{InI}$ with identity matrix \mathbf{I}_{N_y} in Eq. (7), the blip encoding matrix can be derived analytically

$$\mathbf{A}_{c_i, z_i}^{blip} \cdot \mathbf{I}_{N_y} = \mathbf{A}_{c_i, z_i}^{blip} = \text{FFT}\{\Theta_{z_i}\} \otimes \mathbf{I}_{N_y}. \quad (8)$$

Combining all the $\mathbf{A}_{c_i, z_i}^{blip}$ with $z_i = 1, \dots, N_z$, the blip encoding matrix for channel c_i is

$$\mathbf{A}_{c_i}^{blip} = \begin{bmatrix} \mathbf{A}_{c_i, 1}^{blip} & \dots & 0 & \dots \\ 0 & \mathbf{A}_{c_i, 2}^{blip} & \dots & 0 \\ 0 & \dots & \ddots & \dots \\ 0 & \dots & \dots & \mathbf{A}_{c_i, N_z}^{blip} \end{bmatrix}. \quad (9)$$

The projection matrix $\mathbf{A}_{c_i}^{proj}$ described the projection operation due to omitting all partition encoding steps and can be formulated as

$$\mathbf{A}_{c_i}^{proj} = [\mathbf{I}_{N_y}, \mathbf{I}_{N_y}, \dots, \mathbf{I}_{N_y}]. \quad (10)$$

The dimension of $\mathbf{A}_{c_i}^{proj}$ is N_y -by- $[N_y \times N_z]$. Taken $\mathbf{A}_{c_i}^{proj}$, $\mathbf{A}_{c_i}^{blip}$, $\mathbf{A}_{c_i}^{coil}$ and Eq. (3) together, the dimension of \mathbf{A}_{c_i} is N_y -by- $[N_y \times N_z]$. Finally, the forward matrix \mathbf{A} is a vertical concatenation of \mathbf{A}_{c_i} with the dimension of $[N_y \times n_c]$ -by- $[N_y \times N_z]$:

$$\mathbf{A} = [\mathbf{A}_{c_1}; \mathbf{A}_{c_2}; \dots; \mathbf{A}_{c_{n_c}}] \quad (11)$$

Eq. (2) is then whitened to equalize the sensitivity of all channels. The spatially whitened signal equation becomes

$$\mathbf{y}^w(t) = \mathbf{A}^w \mathbf{s}(t) + \mathbf{n}^w(t). \quad (12)$$

Solving the $\mathbf{s}(t)$ in Eq. (12) is an ill-posed inverse problem. One common choice is the minimum-norm estimate (MNE) (Hämäläinen and Ilmoniemi, 1984; Lin et al., 2006). Repeating this inversion procedure over $\mathbf{y}(t)$ of the different frequency encoding indices yields the volumetric reconstruction of dynamic images. Fig. 4 illustrates the procedure of spatial reconstruction.

For each voxel in the reconstructed 3D volume, the hemodynamic response (HDR) is separately estimated by using the standard general linear model (GLM) framework (Friston et al., 1995a, 1995b, 1995c).

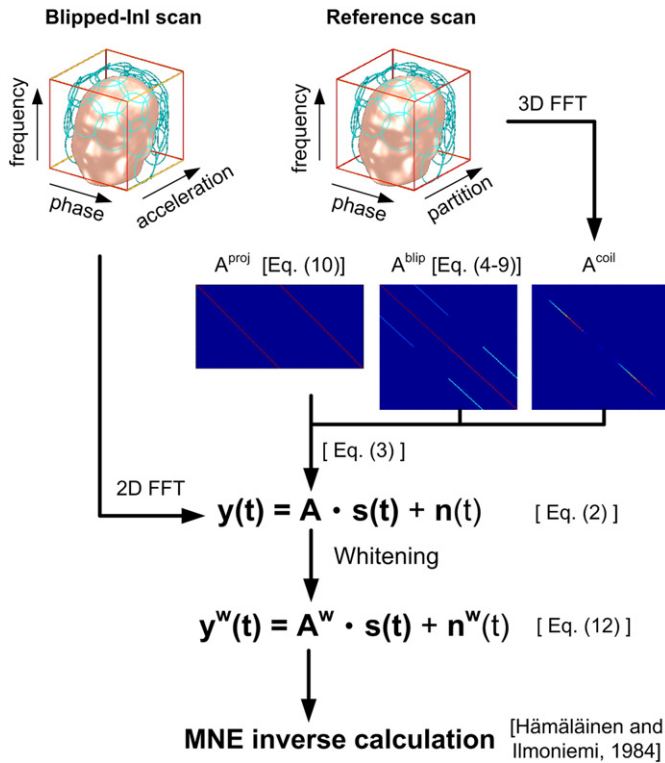


Fig. 4. The flow chart of bInI spatial reconstruction. The acquired k -space data is firstly Fourier transformed to image domain. The forward matrix in Eq. (2), being composed of three encoding matrix, is then constructed. Finally the spatial information is reconstructed by the MNE inversion.

We use finite impulse response (FIR) basis functions to model the HDR to avoid bias in estimating the shape of HDRs. The FIR bases are temporally synchronized to the onsets of the stimuli, spanning over a 30 s period, including a 6 s pre-stimulus baseline and 24 s post-stimulus interval. Since InI/bInI data are sampled at 10 Hz, FIR bases consist of 300 temporally shifted discrete delta functions. To obtain statistical inferences, the noise level of the reconstructed volumetric images is estimated from the pre-stimulus baseline. Using these noise estimates, dynamic statistical parametric maps (dSPM) are derived as the ratio of the MNE values over the baseline noise estimates at each voxel. The dSPM follows a t distribution-like under the null hypothesis of no hemodynamic response (Dale et al., 2000). Since the number of samples used to calculate the noise variance is high (60 in this study), the t distribution approaches the normal distribution and the t -statistics approximates the z -scores.

Materials and methods

Participants

Four healthy participants, with normal or corrected-to-normal vision, were recruited for this study. Informed consent for this study was obtained from each participant in accordance with the experimental protocol approved by the Massachusetts General Hospital Institutional Review Board.

Task

Subjects were instructed to maintain fixation at the center of a screen while viewing a high-contrast visual checkerboard, with contrast-reversing at 8 Hz. The checkerboard subtended 20° of visual angle and was generated from 24 evenly distributed radial wedges (15° each) and eight concentric rings of equal width. The two central concentric rings

were removed to avoid potential blurring of the foveal BOLD signal across hemispheres. The stimuli were presented using Presentation (Version 14.9; Neuro Behavioral Systems, Albany, CA). The reversing checkerboard stimuli were presented for duration of 500 ms and the onset of each stimulus was randomized with the minimum inter-stimulus interval of 2 s. Forty stimuli were presented in three 180-s runs, resulting in a total of 120 stimuli for each participant. Half of the visual stimuli were presented on the left and the other half on the right visual hemifield. In addition, a cross hair was shown in the center of the screen to assist the participant in maintaining eye fixation. The cross hair was occasionally changed to an upside-down “T” for 600 ms and then changed back to a regular cross hair. Within any second, the cross hair changes and checkerboard flashing did not occur synchronously. The participants were instructed to push a button on a response box whenever the crosshair changed, and these responses were recorded to confirm accurate performance and compliance with the task instructions.

Blipped-InI acquisition

Data was collected on a 3 T MRI scanner with a body transmit coil and a 32-channel head receiving coil array (Tim Trio, Siemens Medical Solutions, Erlangen, Germany). To demonstrate the benefit of bInI, for each subject, task data was collected using conventional EPI, InI, and bInI. The InI and bInI acquisitions used EPI frequency encoding along the inferior–superior direction and phase encoding along the left–right direction. A slab-selective RF pulse was used to achieve whole brain magnetization excitation. InI and bInI reconstruction requires a reference scan that provides coil sensitivity maps and allows for the construction of a forward matrix for spatial encoding. InI and bInI replaced partition encoding steps with an image reconstruction algorithm that solves a set of inverse problems along the partition encoding (anterior–posterior) direction to achieve acceleration. Moreover, the bInI reference scan estimated the additional phase shifts introduced in even k -space lines of each partition.

The multi-shot InI reference scan used the following imaging parameters: TR = 100 ms, TE = 30 ms, bandwidth = 2056 Hz/pixel; FOV = $256 \times 256 \times 256 \text{ mm}^3$; image matrix = $64 \times 64 \times 64$; and flip angle = 30° . The bInI reference scan used the same parameters with InI reference scan except the additional z blips which had the gradient moment of $\beta \Delta k_z$. The total acquisition time for the both types of reference scans was 12.8 s with 64 TRs allowing the coverage of a volume comprising 64 partitions with 2 repetitions. For InI and bInI functional scans, we used the same volume prescription, TR, TE, flip angle, and bandwidth as those in the reference scan. The principal difference was that the partition encoding was removed so that a coronal projection image was obtained from each channel of the coil array. The InI and bInI reconstruction algorithm, described in the previous section, was then used to estimate the spatial distribution of magnetization along the anterior–posterior direction. In each run, we collected 1800 measurements after 60 dummy measurements in order to reach the longitudinal magnetization steady state. Totally 3 runs of data were acquired from each participant. In addition to functional scans, resting-state InI and bInI acquisitions were also collected for 1 min to estimate the noise covariance matrix.

For comparison, typical multi-slice EPIs were also acquired with TR = 2 s, TE = 30 ms, flip angle = 90° , bandwidth = 2442 Hz/pixel, FOV = $192 \times 192 \times 115.5 \text{ mm}^3$, and image matrix size = $64 \times 64 \times 33$. Three runs of EPI data were collected. Each run lasted for 3 min.

Anatomical imaging

Structural MRI data for each participant was also collected using a conventional T1-weighted 3D imaging sequence (MPRAGE; TR/TE/TI = 2530/3.03/1100 ms, flip angle = 7° , partition thickness = 1.0 mm, image matrix = 256×224 , 192 partitions, and field-of-view =

25.6 cm × 22.4 cm). Using this data, the gray–white matter boundary for each participant was estimated by FreeSurfer (<http://surfer.nmr.mgh.harvard.edu/>), which uses an automatic segmentation algorithm to yield a triangulated mesh model with approximately 340,000 vertices (Dale et al., 1999; Fischl et al., 2001, 1999). This anatomical model was then used to facilitate mapping of the structural image from native anatomical space to a standard cortical surface space (Dale et al., 1999; Fischl et al., 1999). To transform the functional results into this cortical surface space, InI and bInI reference scans were spatially co-registered with the native space anatomical data using FLIRT (<http://www.fmrib.ox.ac.uk/fsl>), estimating a 12-parameter affine transformation between the volumetric InI reference and the MPRAGE anatomical space. The resulting spatial transformation was subsequently applied to each time point of the reconstructed InI and bInI hemodynamic estimates, to spatially transform the BOLD signal estimates to a standard cortical surface space (Dale et al., 1999; Fischl et al., 1999). We also utilized FreeSurfer to label the subcortical regions of the InI and bInI data to enable evaluation of spatial resolution and localization for the subcortical region, in addition to whole brain evaluation (see section below).

Spatial resolution and localization accuracy evaluation

We performed calculations to quantify the spatial resolution and localization accuracy of InI and bInI reconstructions. The reference scan in each channel of the coil array was synthetically averaged across partitions in order to simulate the InI acquisitions. To simulate bInI acquisition, the blip encoding matrix of every partition (see $\mathbf{A}_{c_i, z_i}^{blip}$ in Eq. (7)) needed to be calculated before spatial integration along the partition encoding direction. To compare between different blip encoding schemes as shown in Fig. 1, we calculated the blip encoding matrices of FOV/2 and FOV/3 cases with blip size of Δk_z . We also calculated the blip encoding matrix of FOV/2 with blip size of Δk_z , $2\Delta k_z$, $4\Delta k_z$, $6\Delta k_z$, to examine the effect of different β . The isocenter is always set at the center of the image volume. The simulated acceleration scan of bInI

was synthesized by averaging across partitions after adding blip phase modulations.

The performance of the reconstruction can be quantified using similar procedure as in MEG source analysis (Chang et al., 2010). The spatial resolution can be estimated by calculating the point spread function (PSF) at each location as

$$PSF_r = \sqrt{\frac{\sum_{r'=1}^{N_y \cdot N_z} |d_{r'}^r \hat{s}_{r'}^r|^2}{\sum_{r'=1}^{N_y \cdot N_z} |\hat{s}_{r'}^r|^2}}, \quad (13)$$

where $d_{r'}^r$ denotes the distance between the true source at the location r and the source estimate at the location r' . $\hat{s}_{r'}^r$ denotes the source estimate at the location r' while the true source is at the location r . PSF_r is the point spread at the location r .

The localization accuracy is evaluated by the SHIFT metric, which is defined as

$$SHIFT_r = \left\{ d_{r_m}^r \mid r_m = \arg \max_{r'} |\hat{s}_{r'}^r| \right\} \quad (14)$$

where $d_{r_m}^r$ denotes the distance between the true source at location r and the maximum source estimate at the location r_m . $SHIFT_r$ is the localization error when the true source is at the location r .

Temporal signal-to-noise ratio (tSNR) measurement

Temporal SNR (tSNR) has been shown to be a good measure of sensitivity to system instabilities and physiological signal variations (Kruger and Glover, 2001; Kruger et al., 2001; Triantafyllou et al., 2005). The first step of tSNR calculation was to calculate the noise covariance from the time series of resting state images. Then we spatially whitened the MR signal such that the noise signals across different

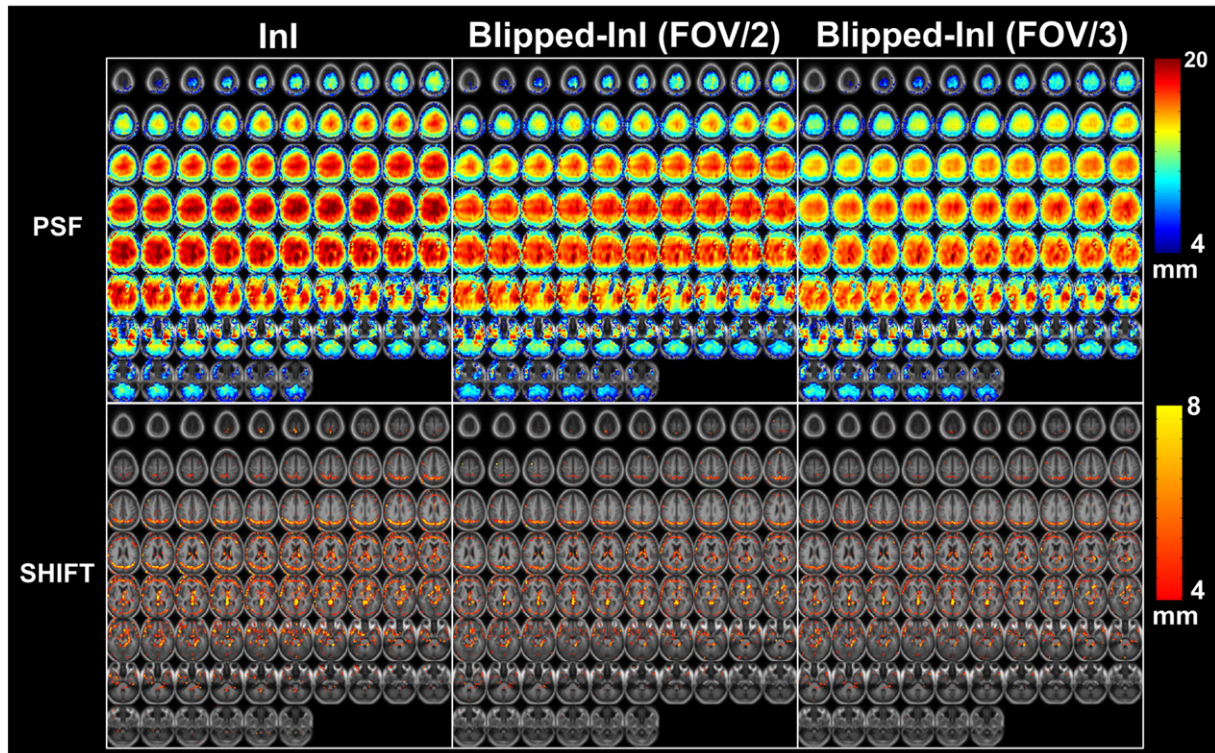


Fig. 5. The group averaged PSF and SHIFT of InI, bInI with FOV/2 shift, and bInI with FOV/3 shift across the whole brain. Higher PSF value implies lower spatial resolution and higher SHIFT value implies lower localization accuracy.

Table 1

The PSFs and SHIFTs of InI, bInI with FOV/2, and bInI with FOV/3. The size of the blip gradient moment of both FOV/2 and FOV/3 is Δk_z . The PSF and SHIFT are averaged either over the whole brain volume or the subcortical regions.

Performance measure (mm)	Whole brain			Subcortical regions		
	InI	FOV/2	FOV/3	InI	FOV/2	FOV/3
PSF	9.9	9.8	9.2	17.1	15.5	15.4
SHIFT	1.6	1.1	1.0	2.8	1.8	1.7

channels were uncorrelated. The mean MR signal intensity of each voxel was averaged over the time series of 50 repetitive frames of signal magnitude. Likewise, the noise variation of each voxel was calculated from the variance of the time series. The voxel-wise MR signal power of each channel was combined using the sum of signal powers of all channels, and noise variation was the sum of noise variances of all channels. The voxel-wise tSNR was the square root of the ratio of signal power to noise variance.

Results

Performance of spatial reconstruction

Fig. 5 shows the group averaged PSF and SHIFT of InI, bInI with spatial shift of FOV/2, and bInI with spatial shift of FOV/3. The minimum magnitude of β in bInI of FOV/2 and FOV/3 is 1. The PSF and SHIFT averaged across i) the whole brain volume and ii) across subcortical regions are listed in Table 1. bInI with FOV/2 and FOV/3 improves the spatial resolution in subcortical regions by 10.5% (1.6 mm) and 10.7% (1.7 mm) when compared to InI, respectively. In addition, bInI with FOV/2 and FOV/3 improves the localization accuracy in the subcortical regions by 54.6% (1 mm) and 68.6% (1.1 mm) respectively. The bInI with FOV/3 provides slightly more improvement than the FOV/2 case at the expense of potentially lengthened readout time due to a larger gradient moment.

Fig. 6 shows the effects of using different gradient moments in the FOV/2 bInI acquisition. The magnitudes of blip gradient moments change between Δk_z , $2\Delta k_z$, $4\Delta k_z$, and $6\Delta k_z$. In general, the improvement by bInI is larger over the subcortical regions than over the cortical regions. Compared to InI, bInI with gradient moments of Δk_z , $2\Delta k_z$,

Table 2

The PSFs and SHIFTs of bInI with FOV/2. The magnitudes of blip gradient moments are Δk_z , $2\Delta k_z$, $4\Delta k_z$ and $6\Delta k_z$, respectively.

Performance measure (mm)	Whole brain				Subcortical regions			
	Δk_z	$2\Delta k_z$	$4\Delta k_z$	$6\Delta k_z$	Δk_z	$2\Delta k_z$	$4\Delta k_z$	$6\Delta k_z$
PSF	9.8	9.5	8.7	8.6	15.5	14.4	12.9	13.4
SHIFT	1.1	0.9	0.8	0.6	1.8	1.5	1.3	1.0

$4\Delta k_z$, and $6\Delta k_z$ improve the spatial resolution in the subcortical regions by 10.5% (1.6 mm), 18.4% (2.7 mm), 32.7% (4.2 mm), and 27.6% (3.7 mm). Likewise, the localization accuracy in the subcortical regions is improved by 54.6% (1.0 mm), 93.3% (1.3 mm), 115.5% (1.5 mm) and 188.2% (1.8 mm) respectively. As the gradient moment increases from 0 to $4\Delta k_z$, the PSF and SHIFT progressively decrease. With the gradient moment of $4\Delta k_z$, the PSF is generally lower than 13 mm and the SHIFT is mostly lower than 2 mm. However, higher gradient moment does not always result in a better condition of forward matrix. As shown in Fig. 6 and Table 2, the spatial resolution in the subcortical regions decreases by 0.5 mm on average if the gradient moment is increased from $4\Delta k_z$ to $6\Delta k_z$, despite an improvement in localization accuracy of 0.3 mm on average.

The improvement of spatial resolution and localization accuracy shall come as a result of improved SNR. To test this hypothesis, we re-constructed both InI and bInI resting-state data. The results in Fig. 7 show that the tSNR of bInI is higher than that of InI, particularly in the center region of the brain. More specifically, the averaged tSNR of bInI over the subcortical regions is 122.3, which is 38.3% higher than that of InI. Likewise, the averaged tSNR of bInI over the cortical surface is 111.6, which is 8.2% higher than that of InI. The spatial pattern of SNR improvement in bInI is consistent with the pattern of improvement in spatial resolution and localization accuracy (Fig. 6).

fMRI experiments

Fig. 8 shows the progressive average of BOLD signal of the conventional EPI, InI and bInI on an inflated cortical surface across four participants. Specifically, the top, middle and bottom rows of Fig. 8

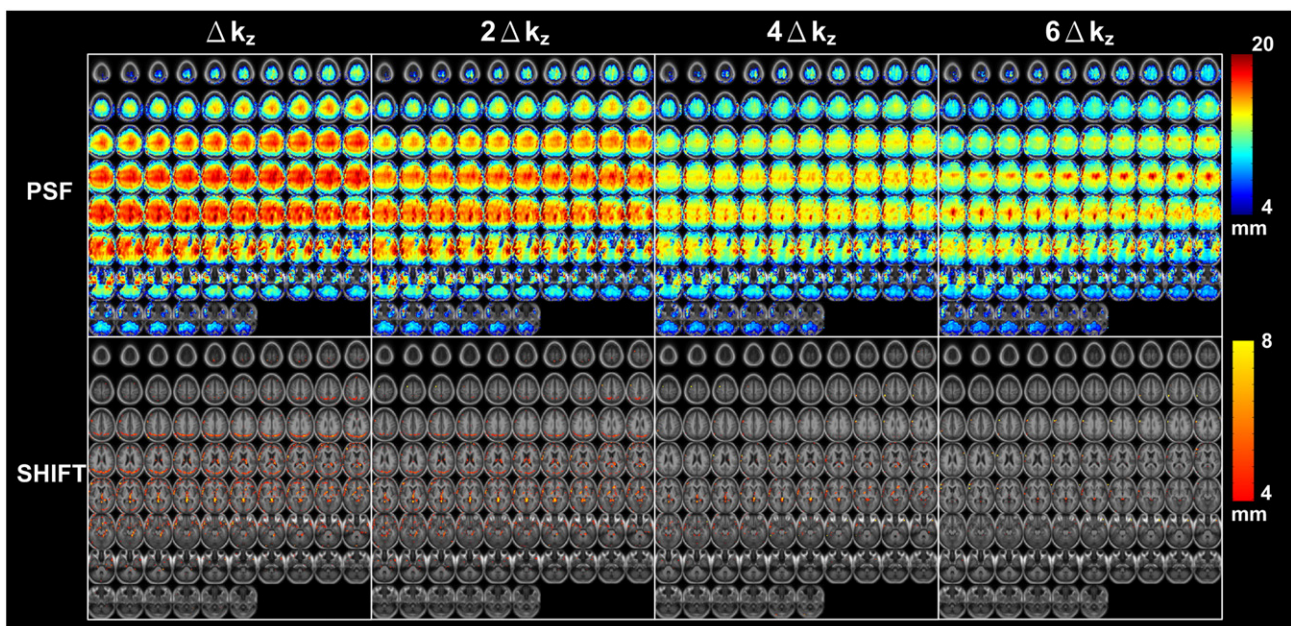


Fig. 6. The group averaged PSF and SHIFT of bInI with blip gradient moments of Δk_z , $2\Delta k_z$, $4\Delta k_z$ and $6\Delta k_z$ respectively. The introduced in-plane shift is FOV/2. A higher PSF value implies lower spatial resolution and a higher SHIFT value implies lower localization accuracy.

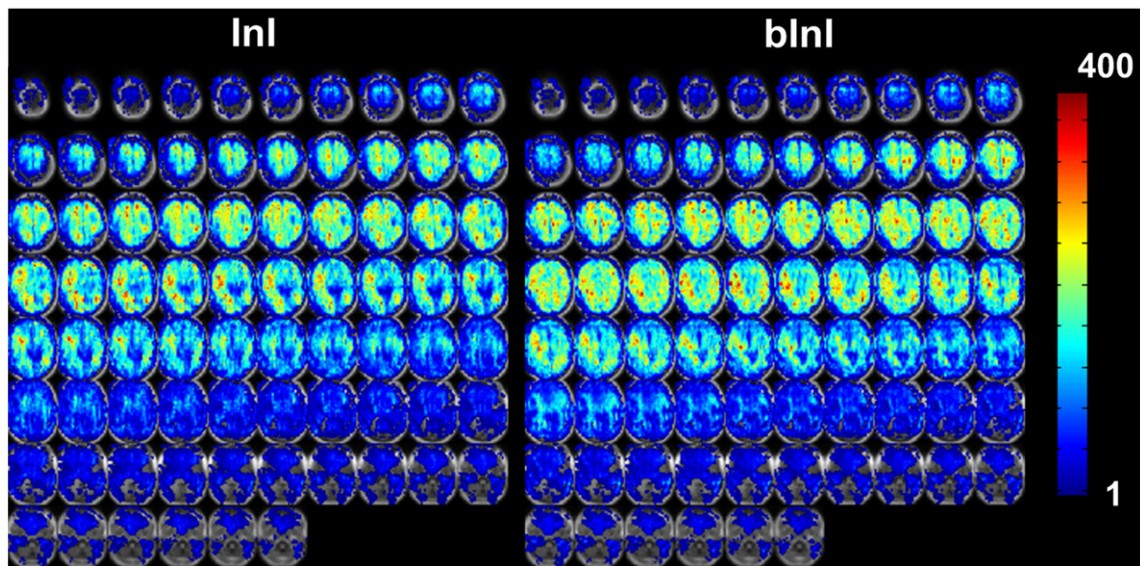


Fig. 7. The tSNR maps of InI and bInI. The values of tSNR are encoded as shown in the color bar. It appears that bInI has higher tSNR than InI around the center of the brain.

respectively show the spatial distributions of the normalized HDR of EPI, InI, and bInI at 4 s after the onset of left hemifield visual stimuli with progressive averaging across four participants. To facilitate better visualization, BOLD signals were scaled so that the maximum and the minimum intensity values represent $\pm 75\%$ of the maximum BOLD signal. Both EPI and bInI exhibit strong BOLD signals and similar spatial distributions. Although InI demonstrates similar BOLD activation with EPI in the visual cortex, the negative BOLD signal shown in the cingulate cortex and the corpus callosum is inconsistent with that of EPI. Blipped InI has no such negative BOLD signal. This result seems to lend support to our simulation data, which suggest that bInI can provide substantial reconstruction improvement in the central part of the brain.

The stimulus-related visual cortex BOLD signal is clearly observed in the group averaged dSPM. Fig. 9 shows snapshots of bInI in the occipital lobe at every 100 ms. These frames show progressively increased BOLD signal starting at 2 s after the left hemifield visual stimuli onset. The signal decreases to baseline approximately 8 s after the stimuli onset. The data in Fig. 9 suggests that bInI can provide spatiotemporal characterization of BOLD signal of the human visual cortex.

Discussion

This work presents a method of inverse imaging (InI) (Lin et al., 2006, 2008) to achieve fast sampling rate (10 Hz with whole brain coverage) in fMRI experiments with improved spatial resolution. InI is fast because of the removal of partition encoding, but has relatively low spatial resolution toward the center of the brain due to insufficient spatial information in channels of a coil array to separate between partitions. Inspired by the blipped-CAIPI method, which utilizes extra slice-selective gradient encoding blips to improve the reconstruction of Simultaneous MultiSlice acquisition, we incorporate these blips into the encoding of InI. The extra slice encoding improves the condition of the forward matrix in the image reconstruction and results in a higher spatial resolution and localization accuracy (Figs. 3 and 4; Tables 1 and 2).

Previously, we proposed the multi-projection InI (mInI) method (Tsai et al., 2012) to improve the spatial resolution of InI by combining data from the InI acquisitions of different projection planes. However, the acquisition of multi-projection InI requires multiple runs and the inverse calculation in 3D space is computationally demanding if more

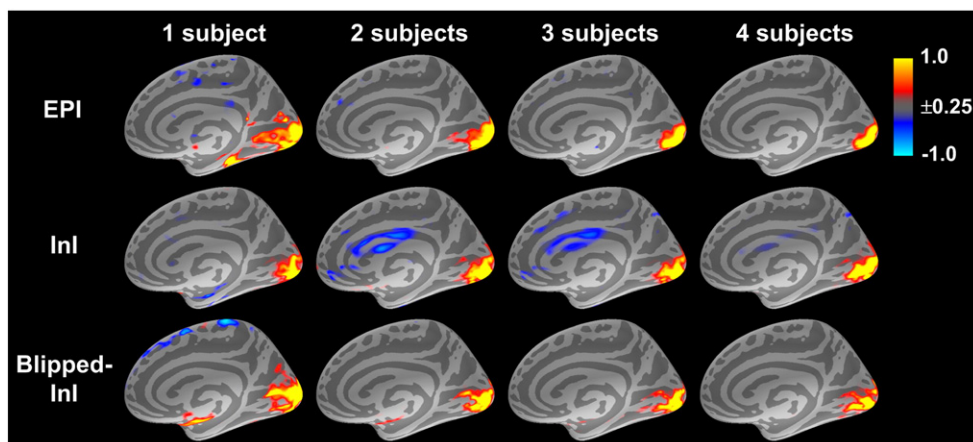


Fig. 8. Maps of BOLD signal at 4 s after the left hemifield visual stimuli onset. From top to bottom rows are the maps of EPI, InI, and bInI, respectively. From left to right columns show the progressive average of 1, 2, 3, and 4 participants. The BOLD signal is linearly scaled so that the '1' in the colorbar represents 75% of the maximum strength of BOLD activation.

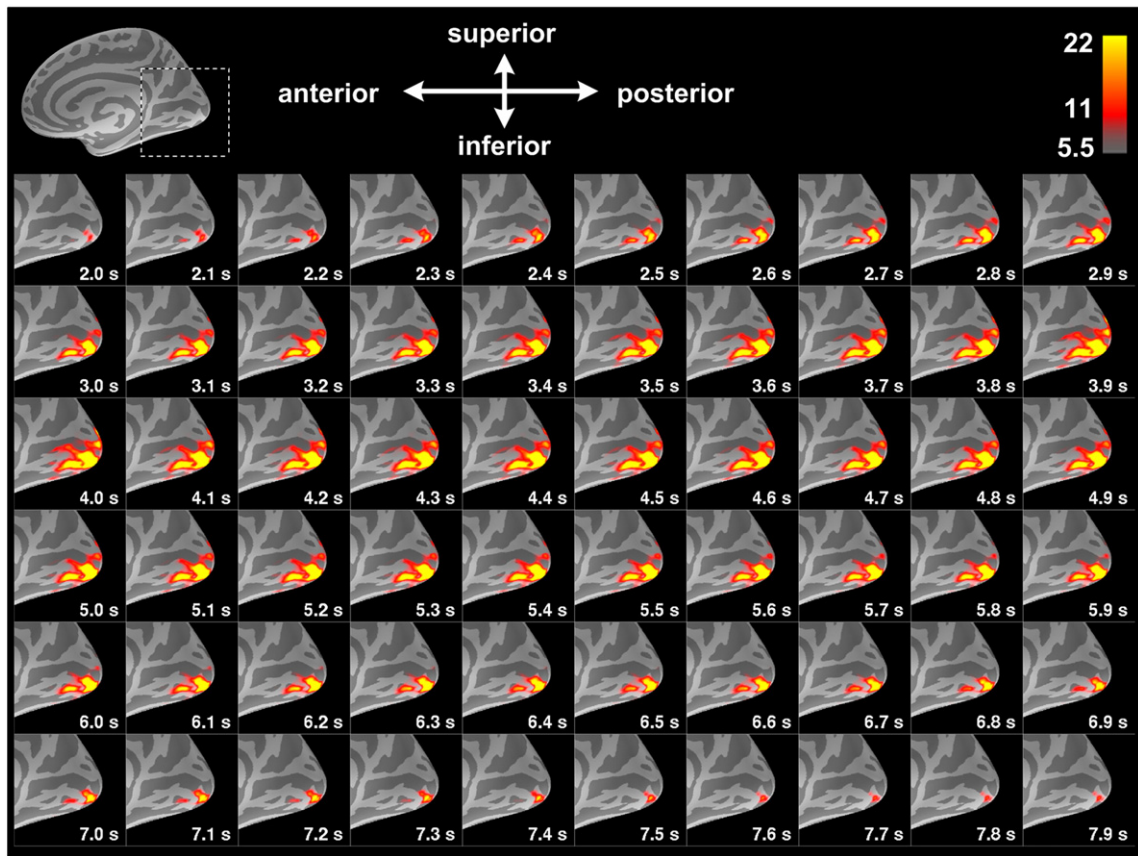


Fig. 9. The group averaged snapshots of the right hemispheric visual cortex DSPMs acquired by bInI. The dashed rectangular box in the figure inset indicates the ROI in the right hemisphere inflated cortical surface. The color bar shows the z-statistics of BOLD signal.

than two projections are used. In contrast, the bInI can improve spatial resolution and localization accuracy of the reconstructed images without using multiple projections. While the spatial resolution improvement is comparable between multi-projection InI and bInI, advantages of bInI over multi-projection InI are i) the feasibility of studying continuous BOLD time series and their correlation and ii) the elimination of concern on motion artifacts between different mInI reference scans across runs. In addition, bInI utilizes the idle time in slice-selection gradient so the addition of slice-selection blips minimally prolong the read-out time and thereby cause neglectable increase in T_2^* blurring.

Blipped InI is similar to the SMS blipped CAIPI because both methods utilize the same gradient encodings in acquisition. The difference between these two methods is that blipped InI replaces a multiband excitation with a slab selective excitation to achieve 3D single-shot imaging. Currently, whole-brain imaging using the SMS blipped CAIPI acquisition requires 4 or 5 shots (with a similar matrix dimension as used in this study). Multi-shot imaging has concerns about the consistency across RF excitations. Blipped InI, on the other hand, has no such concerns.

For standard fMRI studies, the SMS approaches have advantages over the blipped InI method due to their higher and more uniform spatial resolution. For some fMRI studies, however, the research aims at detailed temporal property of hemodynamic responses. For example, animal studies have shown that sequential neuronal activations can modulate the fMRI signal amplitude at a time scale of tens of milliseconds (Ogawa et al., 2000). Such studies may also focus on the time-frequency property (Baria et al., 2011) and inter-regional modulation of hemodynamic responses (Chang et al., 2008; Menon et al., 1998). Additionally, based on numerical simulations from different labs, a faster sampling rate can significantly improve the detection power of effective connectivity (Deshpande et al., 2010; Kayser et al., 2009; Roebroek et al., 2005).

The temporal resolution of 200–300 ms should be adequate for normal fMRI studies to filter a large portion of the physiological noise related to cardiac and respiratory fluctuations. However, a resting heart rate up to 100 bpm is still considered normal. The range can be wider in clinical disorders (Kolloch et al., 2008). To remove these physiological artifacts and their harmonics, the cutoff frequency of a low-pass filter needs to be no lower than 3.3 Hz. In such a case, even a 200 ms/volume sampling rate would not be adequate to completely remove the physiological noise components according to the Nyquist sampling theory.

In our simulation and reconstruction, it was assumed that the phase encodings of the G_z gradient blips are constant across the voxel dimension along the image partition. However, additional linear phase encoding component arises due to finite thickness (Δz) of the image partition. This causes through-partition intra-voxel dephasing, similar to the through-slice dephasing in blipped-CAIPI acquisition, which was previously reported in (Setsompop et al., 2012). This intra-voxel dephasing results in signal attenuation, which can be calculated

as $1 - \frac{1}{\Delta z} \left| \int_{-\Delta z/2}^{\Delta z/2} e^{j2\pi\beta z' / \text{FOV}_z} dz' \right|$. Stronger blip gradient moment, i.e. larger

β , will cause more signal attenuation. For the case of $\beta = 4$ and $N_z = 64$, the signal attenuation is 0.64%. Therefore, the through-partition signal attenuation is very much neglectable if the gradient blip strength is not stronger than $4\Delta k_z$.

An alternative way other than Eq. (3) for constructing the forward matrix is to describe the whole set in k-space sampling (Pruessmann et al., 1999). At each k-space sampling point in each channel of the coil array, the acquired data is the spatial integration of spin density weighted by a spatial encoding function composed of spatial harmonic modulation and RF coil sensitivity. Hence, a forward solution can be

constructed by stacking rows that describe the spatial encoding function at every voxel in the y - z plane. The linear relationship between the k -space sampling and the image to be reconstructed is similar to Eq. (2), except that $\mathbf{y}(t)$ in the image domain is replaced by the k -space acquisition in the frequency domain.

In this study we employed MNE to reconstruct the spatial information but other reconstruction methods can also be considered. On top of the improved condition of the forward matrix in Eq. (2) resulted from additional G_z blip, more sophisticated reconstruction methods, such as linear constrained minimum variance (LCMV) (Lin et al., 2008) and klnl (Lin et al., 2010), are expected to bring further spatial resolution improvement.

In summary, our simulation and experimental results suggest that bInl can be used to reduce spatial blurring and localization error of the Inl method. Through simulation, we demonstrate the effects of various bInl acquisition schemes with different FOV/ n ($n > 2$) shifts and gradient blip sizes. The empirical data from bInl acquisition also exhibits less physiologically unlikely activity in the subcortical regions when compared to the data from Inl acquisition, even when a small blip gradient moment of size Δk_z is used. Based on simulation results, the performance of bInl is expected to improve further with larger gradient blip sizes, such as $4\Delta k_z$. The spatiotemporal pattern of BOLD activation in bInl is also shown to be consistent with the canonical BOLD response. Given its demonstrated benefits, bInl could be a useful tool for investigating human brain function in cortical and subcortical areas at high spatiotemporal resolution.

Acknowledgments

We appreciate the technical support by Mary T. O'Hara and Lawrence T. White at Athinoula A. Martinos Center for Biomedical Imaging. This work was supported in part by Stephanie Rossi. Additionally, this work was supported by the National Institutes of Health (NIH) Grants R01DA14178, R01MH083744, R21DC010060, R01HD040712, R01NS037462, P41 RR14075, R01EB006847, R01EB000790, and R21EB007298, the Mental Illness and Neuroscience Discovery Institute (MIND), NSC 101-2628-B-002-005-MY3 (National Science Council, Taiwan), NSC NSC 100-2325-B-002-046 (National Science Council, Taiwan), NHRI-EX102-10247EI (National Health Research Institute, Taiwan), 100-EC-17-A-19-S1-175 (Ministry of Economic Affairs, Taiwan), and Academy of Finland (the FiDiPro program and grant 127624), Finnish Cultural Foundation, and Finnish Foundation for Technology Promotion. The research environment was supported by the NIH/National Center for Research Resources Shared Instrumentation Grants S1ORR014978, S1ORR021110, S1ORR019307, and S1ORR023401.

References

- Baria, A.T., Baliki, M.N., Parrish, T., Apkarian, A.V., 2011. Anatomical and functional assemblies of brain BOLD oscillations. *J. Neurosci.* 31, 7910–7919.
- Belliveau, J.W., Kennedy Jr., D.N., McKinstry, R.C., Buchbinder, B.R., Weisskoff, R.M., Cohen, M.S., Vevea, J.M., Brady, T.J., Rosen, B.R., 1991. Functional mapping of the human visual cortex by magnetic resonance imaging. *Science* 254, 716–719.
- Breuer, F.A., Blaimer, M., Heidemann, R.M., Mueller, M.F., Griswold, M.A., Jakob, P.M., 2005. Controlled aliasing in parallel imaging results in higher acceleration (CAIPIRINHA) for multi-slice imaging. *Magn. Reson. Med.* 53, 684–691.
- Chang, C., Thomson, M.E., Glover, G.H., 2008. Mapping and correction of vascular hemodynamic latency in the BOLD signal. *Neuroimage* 43, 90–102.
- Chang, W.T., Nummenmaa, A., Hsieh, J.C., Lin, F.H., 2010. Spatially sparse source cluster modeling by compressive neuromagnetic tomography. *Neuroimage* 53, 146–160.
- Chang, W.T., Nummenmaa, A., Witzel, T., Ahveninen, J., Huang, S., Tsai, K.W., Chu, Y.H., Polimeni, J.R., Belliveau, J.W., Lin, F.H., 2013. Whole-head rapid fMRI acquisition using echo-shifted magnetic resonance inverse imaging. *Neuroimage* 78, 325–338.
- Chung, Y.C., Duerk, J.L., 1999. Signal formation in echo-shifted sequences. *Magn. Reson. Med.* 42, 864–875.
- Dale, A.M., Fischl, B., Sereno, M.I., 1999. Cortical surface-based analysis. I. Segmentation and surface reconstruction. *Neuroimage* 9, 179–194.
- Dale, A.M., Liu, A.K., Fischl, B.R., Buckner, R.L., Belliveau, J.W., Lewine, J.D., Halgren, E., 2000. Dynamic statistical parametric mapping: combining fMRI and MEG for high-resolution imaging of cortical activity. *Neuron* 26, 55–67.
- Deshpande, G., Sathian, K., Hu, X., 2010. Effect of hemodynamic variability on Granger causality analysis of fMRI. *Neuroimage* 52, 884–896.
- Feinberg, D.A., Hale, J.D., Watts, J.C., Kaufman, L., Mark, A., 1986. Halving MR imaging time by conjugation: demonstration at 3.5 kG. *Radiology* 161, 527–531.
- Feinberg, D.A., Moeller, S., Smith, S.M., Auerbach, E., Ramanna, S., Gunther, M., Glasser, M.F., Miller, K.L., Ugurbil, K., Yacoub, E., 2010. Multiplexed echo planar imaging for sub-second whole brain fMRI and fast diffusion imaging. *PLoS One* 5, e15710.
- Fischl, B., Sereno, M.I., Dale, A.M., 1999. Cortical surface-based analysis. II: inflation, flattening, and a surface-based coordinate system. *Neuroimage* 9, 195–207.
- Fischl, B., Liu, A., Dale, A.M., 2001. Automated manifold surgery: constructing geometrically accurate and topologically correct models of the human cerebral cortex. *IEEE Trans. Med. Imaging* 20, 70–80.
- Friston, K.J., Frith, C.D., Frackowiak, R.S., Turner, R., 1995a. Characterizing dynamic brain responses with fMRI: a multivariate approach. *Neuroimage* 2, 166–172.
- Friston, K.J., Frith, C.D., Turner, R., Frackowiak, R.S., 1995b. Characterizing evoked hemodynamics with fMRI. *Neuroimage* 2, 157–165.
- Friston, K.J., Holmes, A.P., Poline, J.B., Grasby, P.J., Williams, S.C., Frackowiak, R.S., Turner, R., 1995c. Analysis of fMRI time-series revisited. *Neuroimage* 2, 45–53.
- Griswold, M.A., Jakob, P.M., Heidemann, R.M., Nittka, M., Jellus, V., Wang, J., Kiefer, B., Haase, A., 2002. Generalized autocalibrating partially parallel acquisitions (GRAPPA). *Magn. Reson. Med.* 47, 1202–1210.
- Hämäläinen, M., Ilmoniemi, R., 1984. Interpreting measured magnetic fields of the brain: estimates of current distributions. Helsinki University of Technology, Helsinki, Finland.
- Hennig, J., Zhong, K., Speck, O., 2007. MR-encephalography: fast multi-channel monitoring of brain physiology with magnetic resonance. *Neuroimage* 34, 212–219.
- Jones, R.A., Haraldseth, O., Muller, T.B., Rinck, P.A., Oksendal, A.N., 1993. K-space substitution: a novel dynamic imaging technique. *Magn. Reson. Med.* 29, 830–834.
- Kayser, A.S., Sun, F.T., D'Esposito, M., 2009. A comparison of Granger causality and coherence in fMRI-based analysis of the motor system. *Hum. Brain Mapp.* 30, 3475–3494.
- Kolloch, R., Legler, U.F., Champion, A., Cooper-Dehoff, R.M., Handberg, E., Zhou, Q., Pepine, C.J., 2008. Impact of resting heart rate on outcomes in hypertensive patients with coronary artery disease: findings from the International Verapamil-SR/trandolapril Study (INVEST). *Eur. Heart J.* 29, 1327–1334.
- Kruger, G., Glover, G.H., 2001. Physiological noise in oxygenation-sensitive magnetic resonance imaging. *Magn. Reson. Med.* 46, 631–637.
- Kruger, G., Kastrup, A., Glover, G.H., 2001. Neuroimaging at 1.5 T and 3.0 T: comparison of oxygenation-sensitive magnetic resonance imaging. *Magn. Reson. Med.* 45, 595–604.
- Kwong, K.K., Belliveau, J.W., Chesler, D.A., Goldberg, I.E., Weisskoff, R.M., Poncelet, B.P., Kennedy, D.N., Hoppel, B.E., Cohen, M.S., Turner, R., et al., 1992. Dynamic magnetic resonance imaging of human brain activity during primary sensory stimulation. *Proc. Natl. Acad. Sci. U. S. A.* 89, 5675–5679.
- Lee, A.T., Glover, G.H., Meyer, C.H., 1995. Discrimination of large venous vessels in time-course spiral blood-oxygen-level-dependent magnetic-resonance functional neuroimaging. *Magn. Reson. Med.* 33, 745–754.
- Lee, H.L., Zahneisen, B., Hugger, T., LeVan, P., Hennig, J., 2013. Tracking dynamic resting-state networks at higher frequencies using MR-encephalography. *Neuroimage* 65, 216–222.
- Lin, F.H., Huang, T.Y., Chen, N.K., Wang, F.N., Stufflebeam, S.M., Belliveau, J.W., Wald, L.L., Kwong, K.K., 2005. Functional MRI using regularized parallel imaging acquisition. *Magn. Reson. Med.* 54, 343–353.
- Lin, F.H., Wald, L.L., Ahlfors, S.P., Hamalainen, M.S., Kwong, K.K., Belliveau, J.W., 2006. Dynamic magnetic resonance inverse imaging of human brain function. *Magn. Reson. Med.* 56, 787–802.
- Lin, F.H., Witzel, T., Zeffiro, T.A., Belliveau, J.W., 2008. Linear constraint minimum variance beamformer functional magnetic resonance inverse imaging. *Neuroimage* 43, 297–311.
- Lin, F.H., Witzel, T., Chang, W.T., Wen-Kai Tsai, K., Wang, Y.H., Kuo, W.J., Belliveau, J.W., 2010. K-space reconstruction of magnetic resonance inverse imaging (K-Inl) of human visuomotor systems. *Neuroimage* 49, 3086–3098.
- Lin, F.H., Nummenmaa, A., Witzel, T., Polimeni, J.R., Zeffiro, T.A., Wang, F.N., Belliveau, J.W., 2012. Physiological noise reduction using volumetric functional magnetic resonance inverse imaging. *Hum. Brain Mapp.* 33, 2815–2830.
- Lin, F.H., Witzel, T., Raji, T., Ahveninen, J., Wen-Kai Tsai, K., Chu, Y.H., Chang, W.T., Nummenmaa, A., Polimeni, J.R., Kuo, W.J., Hsieh, J.C., Rosen, B.R., Belliveau, J.W., 2013. fMRI hemodynamics accurately reflects neuronal timing in the human brain measured by MEG. *Neuroimage* 78, 372–384.
- Liou, S.T., Witzel, T., Nummenmaa, A., Chang, W.T., Tsai, K.W., Kuo, W.J., Chung, H.W., Lin, F.H., 2011. Functional magnetic resonance inverse imaging of human visuomotor systems using eigenspace linearly constrained minimum amplitude (eLCMA) beamformer. *Neuroimage* 55, 87–100.
- Lustig, M., Donoho, D., Pauly, J.M., 2007. Sparse MRI: the application of compressed sensing for rapid MRI imaging. *Magn. Reson. Med.* 58, 1182–1195.
- Mansfield, P., 1977. Multi-planar image formation using NMR spin echoes. *J. Phys. C Solid State Phys.* 10, L55–L58.
- McGibney, G., Smith, M.R., Nichols, S.T., Crawley, A., 1993. Quantitative evaluation of several partial Fourier reconstruction algorithms used in MRI. *Magn. Reson. Med.* 30, 51–59.
- Menon, R.S., Luknowsky, D.C., Gati, J.S., 1998. Mental chronometry using latency-resolved functional MRI. *Proc. Natl. Acad. Sci. U. S. A.* 95, 10902–10907.
- Ogawa, S., Lee, T.M., Kay, A.R., Tank, D.W., 1990. Brain magnetic resonance imaging with contrast dependent on blood oxygenation. *Proc. Natl. Acad. Sci. U. S. A.* 87, 9868–9872.
- Ogawa, S., Lee, T.M., Stepnoski, R., Chen, W., Zhu, X.H., Ugurbil, K., 2000. An approach to probe some neural systems interaction by functional MRI at neural time scale down to milliseconds. *Proc. Natl. Acad. Sci. U. S. A.* 97, 11026–11031.

- Posse, S., Ackley, E., Mutihac, R., Rick, J., Shane, M., Murray-Krezan, C., Zaitsev, M., Speck, O., 2012. Enhancement of temporal resolution and BOLD sensitivity in real-time fMRI using multi-slab echo-volumar imaging. *Neuroimage* 61, 115–130.
- Preibisch, C., Pilatus, U., Bunke, J., Hoogenraad, F., Zanella, F., Lanfermann, H., 2003. Functional MRI using sensitivity-encoded echo planar imaging (SENSE-EPI). *Neuroimage* 19, 412–421.
- Pruessmann, K.P., Weiger, M., Scheidegger, M.B., Boesiger, P., 1999. SENSE: sensitivity encoding for fast MRI. *Magn. Reson. Med.* 42, 952–962.
- Roebroeck, A., Formisano, E., Goebel, R., 2005. Mapping directed influence over the brain using Granger causality and fMRI. *Neuroimage* 25, 230–242.
- Särkkä, S., Solin, A., Nummenmaa, A., Vehtari, A., Auranen, T., Vanni, S., Lin, F.H., 2012. Dynamic retrospective filtering of physiological noise in BOLD fMRI: DRIFTER. *Neuroimage* 60, 1517–1527.
- Schmidt, C.F., Degonda, N., Luechinger, R., Henke, K., Boesiger, P., 2005. Sensitivity-encoded (SENSE) echo planar fMRI at 3T in the medial temporal lobe. *Neuroimage* 25, 625–641.
- Setsompop, K., Gagoski, B.A., Polimeni, J.R., Witzel, T., Wedeen, V.J., Wald, L.L., 2012. Blipped-controlled aliasing in parallel imaging for simultaneous multislice echo planar imaging with reduced g-factor penalty. *Magn. Reson. Med.* 67, 1210–1224.
- Sodickson, D.K., Manning, W.J., 1997. Simultaneous acquisition of spatial harmonics (SMASH): fast imaging with radiofrequency coil arrays. *Magn. Reson. Med.* 38, 591–603.
- Triantafyllou, C., Hoge, R.D., Krueger, G., Wiggins, C.J., Potthast, A., Wiggins, G.C., Wald, L.L., 2005. Comparison of physiological noise at 1.5 T, 3 T and 7 T and optimization of fMRI acquisition parameters. *Neuroimage* 26, 243–250.
- Tsai, K.W., Nummenmaa, A., Witzel, T., Chang, W.T., Kuo, W.J., Lin, F.H., 2012. Multi-projection magnetic resonance inverse imaging of the human visuomotor system. *Neuroimage* 61, 304–313.
- Tsao, J., Behnia, B., Webb, A.G., 2001. Unifying linear prior-information-driven methods for accelerated image acquisition. *Magn. Reson. Med.* 46, 652–660.
- van Vaals, J.J., Brummer, M.E., Dixon, W.T., Tuithof, H.H., Engels, H., Nelson, R.C., Gerety, B.M., Chezmar, J.L., den Boer, J.A., 1993. “Keyhole” method for accelerating imaging of contrast agent uptake. *J. Magn. Reson. Imaging* 3, 671–675.
- Witzel, T., Polimeni, J.R., Wiggins, G.C., Lin, F.H., Biber, S., Hamm, M., Seethamraju, R., Wald, L.L., 2008. Single-shot echo-volumar imaging using highly parallel detection. *Proc ISMRM*, p. 1387.
- Witzel, T., Polimeni, J.R., Lin, F.H., Numenmaa, A., Wald, L.L., 2011. Single-shot whole brain echo volume imaging for temporally resolved physiological signals in fMRI. *Proc ISMRM*, p. 633.
- Zahneisen, B., Poser, B.A., Ernst, T., Stenger, V.A., 2013. Three-dimensional Fourier encoding of simultaneously excited slices: generalized acquisition and reconstruction framework. *Magn. Reson. Med.* <http://dx.doi.org/10.1002/mrm.24875> (2013 Jul 22).
- Zientara, G.P., Panych, L.P., Jolesz, F.A., 1994. Dynamically adaptive MRI with encoding by singular value decomposition. *Magn. Reson. Med.* 32, 268–274.